Dominance of goethite over hematite in iron oxides of mineral dust from Western Africa: Quantitative partitioning by X-ray absorption spectroscopy

Paola Formenti, Sandrine Caquineau, Servanne Chevaillier, Anne Klaver, Karine Desboeufs, Jean-Louis Rajot, S. Belin, V. Briois

AGU PUBLICATIONS

JGR

Journal of Geophysical Research: Atmospheres

RESEARCH ARTICLE
10.1002/2014JD021668

Key Points:
- Goethite exceeds hematite in African mineral dust
- Calculation of optical properties in dust models have to be revised

Correspondence to:
P. Formenti,
paola.formenti@lisa.u-pec.fr

Citation:
Formenti, P., S. Caquineau, S. Chevaillier, A. Klaver, K. Desboeufs, J. L. Rajot, S. Belin, and V. Briois (2014), Dominance of goethite over hematite in iron oxides of mineral dust from Western Africa: Quantitative partitioning by X-ray absorption spectroscopy, *J. Geophys. Res. Atmos.*, *119*, 12,740–12,754, doi:10.1002/2014JD021668.

Received 19 FEB 2014
Accepted 8 OCT 2014
Accepted article online 13 OCT 2014
Published online 21 NOV 2014

Dominance of goethite over hematite in iron oxides of mineral dust from Western Africa: Quantitative partitioning by X-ray absorption spectroscopy

P. Formenti[1], S. Caquineau[2], S. Chevaillier[1], A. Klaver[1], K. Desboeufs[1], J. L. Rajot[1,3], S. Belin[4], and V. Briois[4]

[1]LISA, UMR CNRS 7583, Paris XII-Val de Marne University, Paris VII-Denis Diderot University, Institut Pierre Simon Laplace, Créteil, France, [2]LOCEAN–PALEOPROXUS, UMR 7159-IRD-CNRS-UPMC-MNHN, Bondy, France, [3]IEES, UMR IRD 242–IRD–UPMC–CNRS-UPEC-AgroParisTech, Bondy, France, [4]Synchrotron SOLEIL, L'Orme des Merisiers, Saint-Aubin, France

Abstract This paper reports on the X-ray absorption analysis of samples of mineral dust emitted from or transported to Western Africa. We found that iron oxides account, by mass, for 38% to 72% of the total elemental iron. They are composed of minerals in the Fe(III) oxidation state: goethite (FeO•OH) and hematite (Fe_2O_3). The apparent fraction of iron oxide attributed to goethite is higher than hematite regardless of the source region from which the dust originated. The goethite percent content of iron oxides is in the range 52–78% (by mass), the highest values being measured for dust originating in the Sahel. The limited number of samples analyzed and the sample-to-sample variability prevent us from concluding firmly on the regional variability of the goethite-to-hematite ratio. Based on the experimental data on mineralogical composition and on concurrent measurements of the number size distribution, the optical properties of mineral dust have been calculated in a Mie approximation for homogeneous spherical particles. At 550 nm, the single-scattering albedo ω_0 ranges between 0.89 and 0.93, the asymmetry factor g ranges between 0.76 and 0.8 and the mass extinction efficiency k_{ext} varies between 0.5 and 1.1 $m^2\,g^{-1}$; these values are all in the range of those from independent direct measurements. Neglecting the partitioning between hematite and goethite and the assimilation of iron oxides by hematite, as it is often done with models, lowers the single-scattering albedo and increases the asymmetry factor in the UV-visible spectral region below 550 nm. The mass extinction efficiency is insensitive to the nature of the iron oxides but rather responds to variations in the number size distribution. The mineralogy of iron oxides should therefore be taken into account when assessing the effect of mineral dust on climate and atmospheric chemistry, in particular via interactions involving photolysis.

1. Introduction

Mineral dust is emitted in large quantities from arid and semiarid areas of the globe and accounts for approximately 2000 megatons to the annual aerosol emissions at the global scale [*Shao et al.,* 2011]. Once in the atmosphere, mineral dust scatters and absorbs radiation, both at solar and terrestrial wavelengths, thus affecting the Earth-atmosphere radiation balance.

At the global scale, the range of the reported direct radiative effect by light scattering and absorption by mineral dust is −0.56 to +0.1 $W\,m^{-2}$ (net, shortwave + longwave) at the top of the atmosphere (TOA) [*Boucher et al.,* 2013]. However, at the local scale, observations during intense episodes of dust transport, when the aerosol optical depth exceeded 1, have documented that the instantaneous outgoing radiation at the TOA can increase by up to 130 $W\,m^{-2}$ in the shortwave and decrease by up to 30 $W\,m^{-2}$ in the longwave [*Haywood et al.,* 2003; *Highwood et al.,* 2003; *Haywood et al.*, 2005; *Slingo et al.*, 2009; *di Sarra et al.,* 2011].

Shortwave radiation absorption by dust warms the atmosphere and cools the surface, while longwave radiation has the opposite response. *Lau et al.* [2009] have found that a basic "elevated heat pump" feedback mechanism, playing a role in altering the water cycle and climate states of West Africa and the tropical Atlantic, can be initiated by the radiative effect of Saharan dust in the atmosphere if the absorption properties are such that the shortwave absorption exceeds the longwave absorption. These authors found that that is the case for highly absorbing dust with a single-scattering albedo ω_0 below 0.95. For larger ω_0, dust surface cooling can induce a reduction of the Monsoon intensity, therefore in the regional precipitation, as stated by *Solmon et al.* [2008].

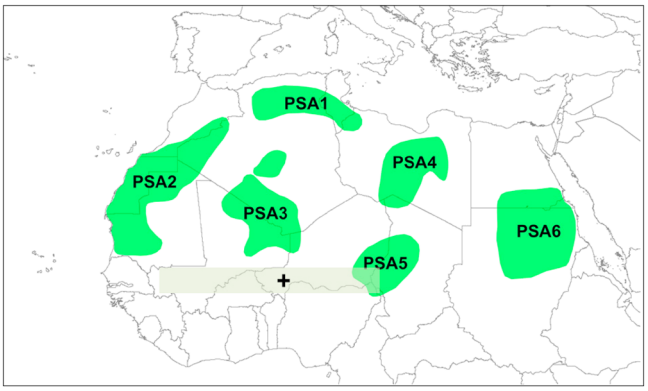

Figure 1. Localization of the Banizoumbou ground-based site, Niger (cross) superimposed on the map of the major potential source areas (PSA) identified by *Scheuvens et al.* [2013]. The approximate localization of the Sahelian dust sources is also indicated. Figure reproduced from *Scheuvens et al.* [2013] with permission from Elsevier.

However, the shortwave absorption properties of mineral dust are debated. A number of measurements, in situ and by remote sensing, indicate that dust is less absorbing than previously considered based on optical analysis of the mineralogical composition [*Patterson et al.,* 1977; *Dubovik et al.,* 2002; *Sinyuk et al.,* 2003; *Haywood et al.,* 2003; *McConnell et al.*, 2008; *Otto et al.*, 2009; *Formenti et al.,* 2011; *Ryder et al.*, 2013]. Recent modeling efforts have revised the description of the shortwave dust optical properties to take these experimental data into account [*Shi et al.,* 2005; *Balkanski et al.,* 2007]. Model calculations were based on two hypotheses: (i) iron oxides are the major absorbing species in the shortwave and (ii) iron oxides can be represented by only one mineralogical species, hematite (Fe_2O_3). However, on a column-closure experiment, *McConnell et al.* [2010] have shown that closure of measured broadband shortwave radiative fluxes (both downwelling and upwelling) is best achieved when the radiative calculations are initiated by assimilating the absorption properties of iron oxides to those of goethite (FeO•OH), the most widely distributed iron oxide in soils [*Schwertmann*, 1971].

In fact, hematite and goethite, both in the Fe(III) oxidation state, are the major iron oxide species in mineral dust [*Torrent et al.,* 1983] and control its absorption properties toward shortwave radiation [e.g., *Sokolik and Toon*, 1999; *Arimoto et al.,* 2002; *Claquin et al.,* 1999; *Lafon et al.,* 2006]. They have distinct optical properties in the shortwave, both in terms of intensity and spectral dependence [*Bedidi and Cervelle,* 1993]. Between 460 and 700 nm, the imaginary part of the complex refractive index (representing absorption) of goethite is up to 3 times lower than that of hematite. The spectral dependence is pronounced for hematite, for which the imaginary part of the refractive index decreases almost monotonically between 0.35 at 460 nm and 0.15 at 700 nm. For goethite, the imaginary part of the complex refractive index varies between 0.07 and 0.10 except at 520 and 680 nm where it presents a band-like structure with absorption reaching 0.13. As a consequence, the apportionment of hematite and goethite in mineral dust can potentially change the magnitude and the spectral dependence of shortwave absorbing properties of mineral dust.

To date, however, only a few, semiquantitative assessments of the partitioning between hematite and goethite in dust aerosols exist, and they are based on visible spectroscopy on aerosol particles collected on filters [*Arimoto et al.,* 2002; *Lafon et al.,* 2006; *Formenti et al.*, 2008] or on mapping of the soil mineralogical composition [*Journet et al.,* 2014].

This paper presents new quantitative data on the distribution of hematite and goethite in African mineral dust; this is relevant to establishing its light absorption properties, hence its direct effect on the radiation balance. This research is based on X-ray absorption analysis of dust samples collected in Niger during winter and summer 2006 in the framework of the African Monsoon Multidisciplinary Analyses (AMMA) program [*Redelsperger et al.,* 2006]. Niger is in the core of the Sahel and experiences local emissions mainly at the beginning of the rainy season [*Marticorena et al.*, 2010]. It is also situated downwind of some of the most persistent Saharan dust sources at the global scale: the Bodélé depression in Chad, the areas in the North of Mali and the south of Algeria, but also those in Libya, Egypt, and Sudan [*Prospero et al.,* 2002; *Laurent et al.,* 2008; *Rajot et al.,* 2008; *Washington et al.,* 2006].

2. Methods

2.1. Sample Collection and Handling

The field samples discussed in this paper were collected at the ground-based site of Banizoumbou (13.5°N; 2.6°E, 250 m above sea level), a remote location at approximately 60 km east of the capital of Niger, Niamey (Figure 1).

Table 1. General Information on Sampling Times and Origin for the Samples Analyzed in This Work[a]

Sample ID	Start Date and Time (Local)	Stop Date and Time (Local)	Origin	Smectite
SOP0-4	15/01/2006 09:09	15/01/2006 14:45	PSA5 (Bodélé)	N
SOP0-5	15/01/2006 15:56	16/01/2006 08:54	PSA5 (Bodélé)	Y
SOP0-29	29/01/2006 19:22	30/01/2006 07:35	PSA3 + North Niger	N
SOP0-31	30/01/2006 13:13	31/01/2006 09:17	PSA3 + North Niger	Y
SOP0-38	03/02/2006 17:01	04/02/2006 09:45	PSA3	Y
SOP0-46	08/02/2006 10:30	09/02/2006 09:15	PSA3 + traces of Sahelian dust from local erosion	Y
SOP1-15	08/06/2006 10:29	08/06/2006 19:19	PSA3 + traces of Sahelian dust from local erosion	N
SOP1-17	08/06/2006 22:33	09/06/2006 06:40	Sahelian dust, posterosion	N
SOP1-19	10/06/2006 14:40	11/06/2006 11:00	PSA5 (Bodélé/Sudan)	N
SOP1-22	13/06/2006 11:47	13/06/2006 17:23	PSA5 (Bodélé/Sudan)	Y
SOP1-37	23/06/2006 12:46	23/06/2006 12:56	Sahelian dust, local erosion	N
SOP1-48	01/07/2006 23:50	02/07/2006 00:02	Sahelian dust, local erosion	N

[a]PSA indicates major potential source areas (PSA) identified by *Scheuvens et al.* [2013] and shown in Figure 1.

Sample collection was conducted during two of the AMMA Special Observing Periods (SOPs): in the winter, between 13 January and 13 February 2006, and in the summer, between 31 May 2006 and 17 July 2006.

These field samples correspond to the collection of dust either transported from Saharan sources or emitted locally in Banizoumbou or in close proximity (Table 1). Transported samples represent a diversity of origins, including the Bodélé depression, whose emissions were sampled during both seasons. Three episodes of native local emission of Sahelian dust were also sampled and characterized [*Formenti et al.,* 2011]. The attribution of origin for remote sources was made using a number of indicators (elemental composition, back trajectories, emission maps, and satellite images) as described in *Rajot et al.* [2008] and *Formenti et al.* [2014].

Aerosol sampling was performed using two identical wind-oriented inlets designed purposefully for the AMMA field campaigns [*Rajot et al.,* 2008]. The cutoff diameter 50% efficiency of these inlets was calculated to be approximately 40 μm by using the standard formulae of particle losses in inlets and tubing as reported in *Baron and Willeke* [2001] and *Hinds* [1999]. Samples were collected on acid-washed 47 mm polycarbonate Nuclepore filters (0.4 μm pore size) mounted on plastic rings and stored in Petri dishes before and after sampling. As indicated in Table 1, sampling time was on the order of hours, and the duration varied depending on the aerosol mass concentration measured online by a Tapered Element Oscillating Microbalance (Rupprecht and Patashnick, Albany, USA) [*Rajot et al.,* 2008].

2.2. Standard Samples

According to concurrent X-ray diffraction measurements [*Formenti et al.,* 2014], Fe in the field samples was associated with iron oxides, illite, and smectites.

Therefore, five mineral standards representing Fe(III)-bearing minerals were chosen (Table 2):

1. A standard sample of illite from Le Puy, France, with a relatively high structural Fe content (5% by mass) and an iron oxide content of $<0.1\%$ [*Van Olphen and Fripiat*, 1979].
2. Natural standards of goethite and hematite, from Minnesota and Niger, respectively.

Table 2. Information on Mono, Binary, and Ternary Mineral Standards Used in This Work

Standard	Stoichiometric Formula	Origin, Provider	Iron Content (%)
Illite du Puy	$(Si_{3.55}Al_{0.45})(Al_{1.27}Fe_{0.36}Mg_{0.44})O_{10}(OH)_2(Ca_{0.01}Na_{0.01}K_{0.53}X(I)_{0.12})$[a]	Puy, France	5
Goethite	FeO OH	Minnesota (WNSE)	63
Hematite	Fe_2O_3	Niger (IRD)	57
Montmorillonite	$(Na,Ca)_{0,3}(Al,Mg)_2Si_4O10(OH)_2 \cdot n(H_2O)$	Osage, Wyoming (WNSE)	2.6
Nontronite	$Na_{0.3}Fe_2(Si,Al)_4O10(OH)_2 \cdot nH2O$	Allentown, Pennsylvania, (WNSE)	23
H50G50	Binary mixture of 50% hematite and 50% goethite (by mass)	----	67
H25G75	Binary mixture of 25% hematite and 75% goethite (by mass)	----	65
I30G30H30	Ternary mixture of 30% illite, 30% hematite, and 30% goethite (by mass)	----	45

[a]X refers to an exchangeable cation with a composition 93% Na, 3% K, and 2% Ca. IRD = Institut de la Recherche pour le Développement and WNSE = Ward's National Science Establishment.

3. A nontronite standard representing a Fe-rich smectite, and a montmorillonite standard representing a Fe-poor smectite.

The Fe content in these standards was determined experimentally by wavelength dispersive X-ray Fluorescence analysis [*Journet et al.,* 2008].

Standards were prepared either as deposit on Nuclepore filters or as pressed pellets diluted to $<5\%$ total Fe (by mass) in quartz to mimic the matrix of a natural dust sample. In the same way, we prepared binary or ternary mixtures of hematite, goethite, and illite where the standards were mixed in known proportions and that we used as control. These are listed in Table 2.

2.3. Sample Analysis

2.3.1. Quantification of Fe Oxide Content

The Fe oxide content, defined as the fraction of Fe that is not in the framework of the crystal structure of silicates [*Karickhoff and Bailey*, 1973], was determined by applying the classical extraction method of *Mehra and Jackson* [1960] for soil analysis in the form adapted by *Lafon et al.* [2004] to aerosol filters. This method typically produced a sampled mass smaller than 500 μg.

The *Mehra and Jackson* [1960] extraction method uses a Citrate-Bicarbonate-Dithionite (CBD) reagent to dissolve iron oxides selectively via reduction.

The Fe oxide content was estimated as the difference of total Fe content in the samples measured by wavelength dispersive X-ray fluorescence analysis [*Lafon et al.,* 2004] prior to and after dissolution. We used a PW-2404 spectrometer by PANalytical. Excitation X-rays are produced by a Coolidge tube ($I_{max} = 125$ mA, $V_{max} = 60$ kV) with a Rh anode; the primary X-ray spectrum can be controlled by inserting filters (Al, at different thicknesses) between the anode and the sample. The full experimental details of these analyses are reported in *Formenti et al.* [2008].

2.3.2. Speciation of Iron Oxides

The speciation of iron oxides was investigated by X-ray absorption (XAS) at the Fe K-edge. As described in *Wilke et al.* [2001] and *O'Day et al.* [2004], the oxidation state and the bonding environment of Fe in dust samples give rise to different features in the XAS spectra, in particular:

1. In the preedge region, the shape of the XAS spectra is determined by electronic transitions to empty bound states, which are strongly influenced not only by the oxidation state of the absorbing atom but also by the local geometry around the absorbing atom due to hybridization effects. *Wilke et al.* [2001] found that for Fe(II)-bearing minerals the position of the centroid of the preedge is found at 7112.1 eV, whereas it is at 7113.5 eV for Fe(III)-bearing minerals.
2. In the edge region, which defines the ionization threshold to continuum state, the position of the rising edge, which depends as well on the oxidation state, is found at approximately 7120 eV.
3. In the X-ray Absorption Near Edge Structure (XANES) region, extending approximately 50 eV above the K-edge peak, whose features are determined by multiple-scattering resonances of the photo-electron ejected at low kinetic energies.

The XAS analysis of mineral dust samples described in this paper was performed at the SAMBA (Spectroscopies Applied to Materials based on Absorption) line at the SOLEIL synchrotron facility in Saclay, France [*Briois et al.,* 2011].

Samples were mounted in an external setup mode. A Si(111) double-crystal monochromator was used to produce a monochromatic X-ray beam with 400 mA maximum current and $200 \times 200\ \mu m^2$ in size. The energy range was scanned from 7000 eV to 7800 eV at a resolution varying between 0.2 eV in proximity to the Fe-K absorption edge (at 7112 eV) and 2 eV in the extended range. Samples were analyzed in the fluorescence mode without prior preparation. The analysis was repeated three times to improve the signal-to-noise ratio. Each analysis lasted approximately 30 min.

Data reduction was performed using the Athena IFEFFIT freeware analysis program, which is available for download at http://cars9.uchicago.edu/ifeffit/BruceRavel/Horae [*Ravel and Newville*, 2005]. The Fe speciation was obtained by the least squares fit of the measured XANES spectra based on the linear combination of the reference spectra, weighted by an α_i coefficient (the index representing the mineral standard), and varied until the best fit of the measured signal is achieved. The "best" α_i weights obtained from fitting are interpreted as apparent component fractions of Fe that can be compared to the expected atomic mass

fractions of Fe in each Fe-bearing mineral. The error on the estimated apparent component fractions of Fe was assumed to be equal to the error returned on each α_i weight by the linear fit procedure. The relative goodness of fir for the linear regression is estimated from the reduced χ^2.

According to *O'Day et al.* [2004], fitting of the first derivatives of the normalized spectral absorbance was preferred in order to take advantage of the spectral variability of the absorbance. Linear combination fits were performed on 296 data points (in terms of energy, between 7108 and 7166 eV; i.e., between −20 and +50 eV of the K-edge). The α_i weights were constrained to vary between 0 and 1 and to sum equal to 1. The energy axis was allowed to vary to compensate for small variations during the analysis.

2.4. Optical Calculations

To assess the importance of the goethite/hematite apportionment on the optical properties relevant to the aerosol direct radiative effect, sensitivity calculations were performed. The calculated optical properties are the spectral mass specific extinction (k_{ext}, expressed in $m^2\,g^{-1}$), the single-scattering albedo ω_0, and the asymmetry factor g [*Chýlek and Wong*, 1995], defined as

$$k_{\text{ext}} = \frac{\sigma_e}{M} \tag{1a}$$

$$\omega_0 = \frac{\sigma_s}{\sigma_s + \sigma_a} \tag{1b}$$

$$g = \frac{1}{2}\int_0^{\pi} \cos\theta P(\theta)\sin\theta \mathrm{d}\theta \tag{1c}$$

where σ_e, σ_s, and σ_a are the particle volume extinction, scattering, and absorption coefficients (units Mm^{-1}, i.e., $10^{-6}\,m^{-1}$), respectively, M is the aerosol mass concentration (expressed in $\mu g\,m^{-3}$), $P(\theta)$ is the angular distribution of scattered light (the phase function), and θ is the light scattering angle [*Bohren and Huffman*, 1983].

These optical properties depend on wavelength, as well as on the aerosol composition, size distribution, and shape. In the approximation of homogeneous spherical particles, they can be written as

$$\sigma_e = \int \pi\ r^2\ Q_e(m,r)\frac{\mathrm{d}N}{\mathrm{dlog}r}\mathrm{dlog}r \tag{2a}$$

$$\sigma_s = \int \pi\ r^2\ Q_s(m,r)\frac{\mathrm{d}N}{\mathrm{dlog}r}\mathrm{dlog}r \tag{2b}$$

$$\sigma_a = \int \pi\ r^2\ Q_a(m,r)\frac{\mathrm{d}N}{\mathrm{dlog}r}\mathrm{dlog}r \tag{2c}$$

where $\mathrm{d}N/\mathrm{dlog}r$ is the number size distribution in particle radius r, m is the particle complex refractive index depending on particle composition, and Q_s and Q_a are the single-particle scattering and absorption efficiencies, respectively [*Bohren and Huffman*, 1983].

Calculations were performed for those samples for which we had been able to assess both the full mineralogical composition [*Formenti et al.*, 2014] and the number size distribution. This was measured in the range 0.3–17 μm in equivalent optical diameter (nominal values) by an optical particle counter (GRIMM Inc., model 1.108). The measured size distributions were parameterized by a log-fit curve representing nine lognormal modes described according to

$$\frac{\mathrm{d}N}{\mathrm{dlog}\,r} = \sum \frac{N_{\text{tot},i}}{\sqrt{2\pi}\,\log\sigma_{g,i}} \exp\left(-\frac{\left(\log r - \log r_{g,i}\right)^2}{2\log^2\sigma_{g,i}}\right)$$

where $r_{g,i}$ represents the median diameter, $\sigma_{g,i}$ is the geometric standard deviation, and $N_{\text{tot},i}$ is the total aerosol number concentration of the i mode [*Seinfeld and Pandis*, 1997]. Calculations were performed based on the hypothesis that minerals are in internal mixing. The complex refractive index m has thus been calculated in the volume-mixed approximation as

$$m = \sum_i f_i\, m_i$$

where f_i and m_i represent the volume fraction and the complex refractive index for the mineral i, respectively [*Bohren and Huffman*, 1983]. The volume fractions were calculated from the measured mass fractions assuming the following mass densities: 2.65 g cm^{-3} for illite, kaolinite, quartz, and calcite, 4.28 g cm^{-3} for goethite, and 5.25 g cm^{-3} for hematite [*Formenti et al.*, 2014]. The complex refractive indices used for each

Table 3. Complex Refractive Indices of Individual Minerals Used in This Study[a]

Mineral	Reference	Spectral Domain (μm)
Illite	*Egan and Hilgeman* [1979]	0.185–2.6
Kaolinite	*Egan and Hilgeman* [1979]	0.185–2.6
Calcite	*Querry et al.* [1978]	0.2–25
Dolomite	*Barthelmy* [2007]	0.185–2.5
Albite	*Barthelmy* [2007]	0.185–2.5
Orthose	*Barthelmy* [2007]	0.185–2.5
Gypsum	*Barthelmy* [2007]	0.185–2.5
Goethite	*Bedidi and Cervelle* [1993]	0.46–0.7
Hematite	*Bedidi and Cervelle* [1993]	0.4–0.7
Quartz	*Longtin et al.* [1988][b]	0.2–2

[a]The spectral domains are indicated.
[b]*Longtin et al.* [1988] have compiled values of complex refractive indices for quartz based on different sources.

mineral are referenced in Table 3. The internal mixing assumption is clearly an approximation as minerals, except iron oxides, are mostly in external mixing [*Formenti et al.,* 2014]. However, this assumption has the advantage of simplicity of calculation, interpretation, and the possibility of comparing with model results.

Calculations were performed at discrete wavelengths (440, 660, and 870 nm) coinciding with those of the Sun photometers of the Aerosol Robotic Network (AERONET) [*Holben et al.*, 1998] and those (450 and 550 nm) of in situ instruments, such as the integrating nephelometer, the aethalometer and the Particle Soot Absorption Photometer [e.g., *Anderson et al.*, 1996; *Formenti et al.,* 2011; *Ryder et al.*, 2013], commonly used in field campaigns on mineral dust, as well as at 370 nm, where hematite absorbs most strongly.

3. Results and Discussion

3.1. Quantification of Hematite and Goethite in Mineral Dust Samples

The normalized XANES spectra and the corresponding first derivatives are shown in Figure 2 for both the natural and the standard samples. The spectral behavior of the natural samples is rather uniform.

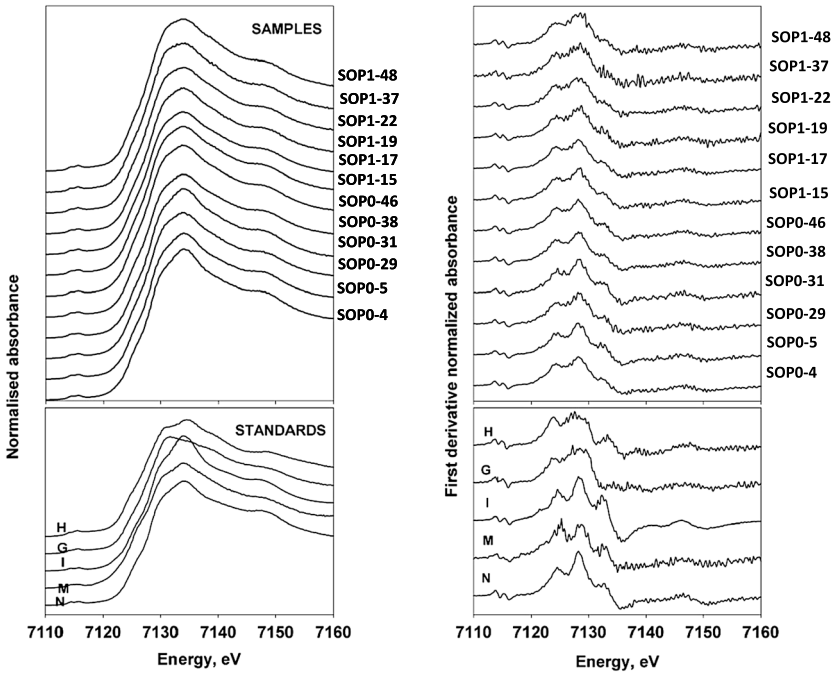

Figure 2. XANES spectra of (left) the normalized absorbance and (right) its first derivative (top) for the dust samples and (bottom) for the monomineral standards. The monomineral standards are identified by their first letter (H = hematite, G = goethite, I = illite, M = montmorillonite, and N = nontronite). Spectra are represented in arbitrary units on a linear scale.

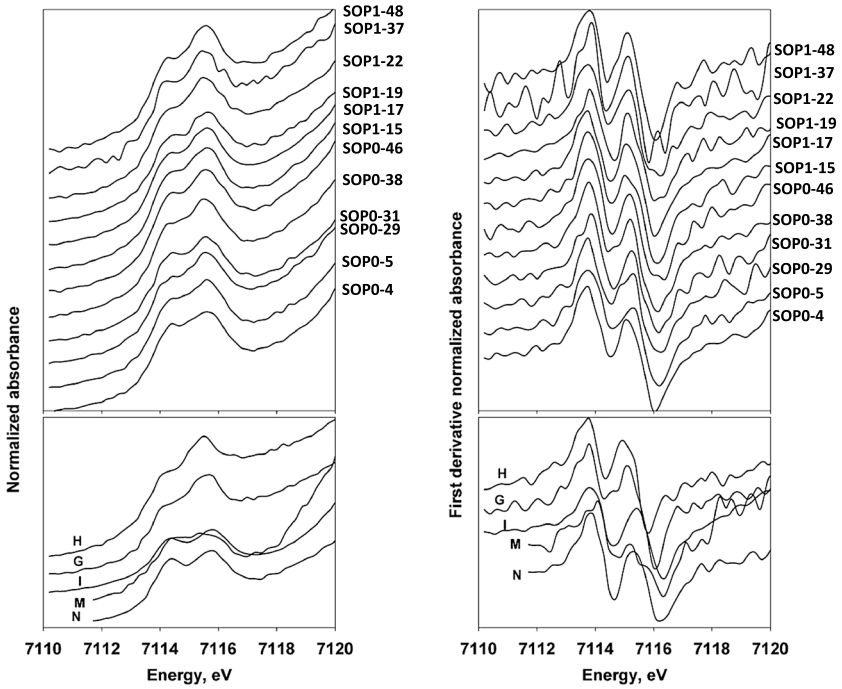

Figure 3. XANES spectra of (left) the normalized absorbance and (right) its first derivative in the preedge region (top) for the dust samples and (bottom) for the monomineral standards. The monomineral standards are identified by their first letter (H = hematite, G = goethite, I = illite, M = montmorillonite, and N = nontronite). Spectra are represented in arbitrary units on a linear scale.

Nonetheless, some distinctive features can be identified. A double-peak structure corresponding to the edge region is found at 7124 and 7128 eV on the first derivative spectra. This is also evident in the monomineral standards, albeit with different peak heights depending on the mineral. As an example, the intensity of the two peaks is almost equal for montmorillonite, whereas the first peak is less intense than the second in the case of illite. A second peak in the XANES region between 7132 and 7136 eV is also evident for samples of dust originating from PSA3 and PSA5 but is almost indistinguishable for samples of Sahelian dust (SOP1-17, SOP1-37, and SOP1-48). This feature is distinctive for all monomineral standards, except goethite.

Figure 3 provides a closer look at the preedge region, again for both the normalized XANES spectra and the corresponding first derivatives. The preedge region of the natural samples is characterized by a double-peak structure due to the 1 s → 3d/4p transition [*Dräger et al*., 1988]. Centroids are positioned between 7114 and 7115.8–7116 eV, indicating that iron is found exclusively in the Fe(III) oxidation state [*Wilke et al.,* 2001]. The intensity of the centroid peaks is modulated by the mixing of the different sixfold structures of the mineral phases. When looking at the standards, the amplitude of second peaks is indeed more pronounced for hematite and goethite with respect to the group containing illite-nontronite and montmorillonite. This is due to the increased distortion of the octahedral structure of the O atoms around Fe(III) [*Wilke et al.,* 2001].

The iron oxide apportionment was first tested by the least squares linear combination fit of the first derivatives of XANES normalized absorbance spectra of the binary or ternary standard mixtures between hematite, goethite, and illite (Figure 4). As shown in Table 4, the comparison of the expected and the estimated relative proportions of Fe is within 9%, which is within one standard deviation regardless of the mixture.

The results of the Fe apportionment of the natural samples are shown in Table 5. The apportionment model was adapted to the knowledge of the mineralogical composition of the samples obtained independently by X-ray diffraction (XRD): for samples not containing smectites (SOP0-4, SOP0-29, SOP1-15, SOP1-17, SOP1-19, SOP1-37, and SOP1-48), the apportion model included illite, hematite, and goethite only. When smectite clays had been detected by XRD (samples SOP0-5, SOP0-31, SOP0-38, SOP0-46, and SOP1-22), we performed two calculations with a four-component model, one considering nontronite and a second considering montmorillonite to represent the possible bounds of variability in this clay type that we are unable to quantify.

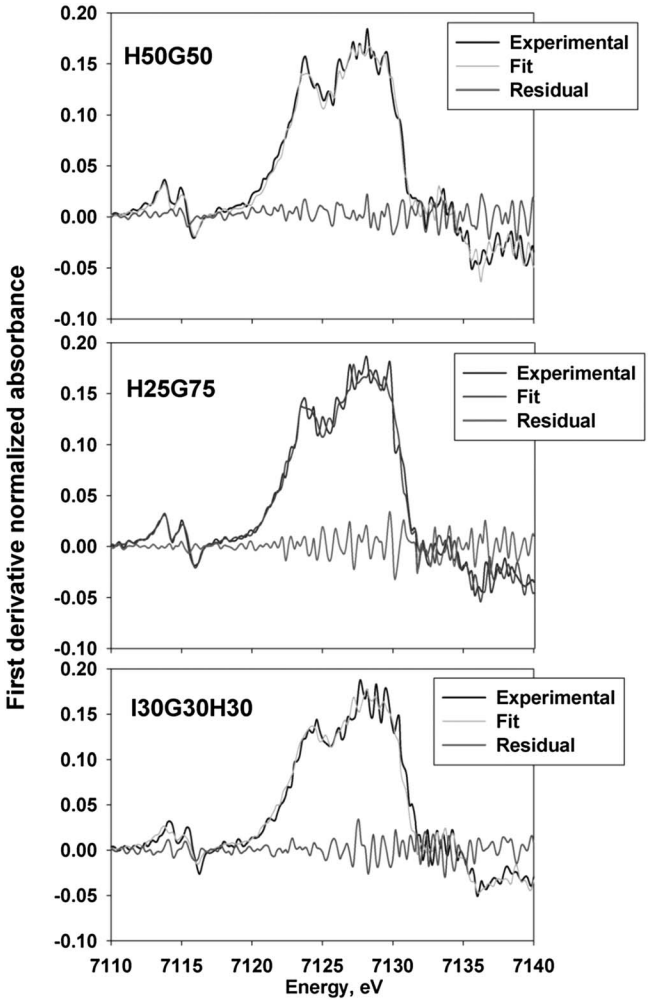

Figure 4. Least squares linear combination fit of the binary or ternary mixtures between hematite, goethite, and illite (H50H50, H25G75, and I30G30H30, see Table 2). Lines represent the experimental first derivative of the normalized absorbance (black), the least squares linear combination fit (light gray), and the residual curve (dark gray).

Depending on the sample, the apparent fraction of Fe to be attributed to hematite varies between 9% (±3%) and 26% (±3%), and between 21% (±2%) and 49% (±3%) for goethite. Goethite is henceforth the dominant species of iron oxides for all samples. Differences in the estimates of the apparent fractions of Fe associated with goethite and with hematite and related to the choice of the deconvolution model are smaller than 6% and 12%, respectively. These are higher for hematite, which has inflection points closer to those of clays than goethite (see Figures 2 and 3). Nonetheless, the relative proportions of hematite and goethite are conserved even when taking these uncertainties into account. The uncertainty in representing the clay type and in apportioning the Fe associated with it does not interfere with the apportionment of Fe in the oxide form.

The apparent fractions of Fe from hematite and goethite can be summed to estimate the apparent fraction of Fe attributable to iron oxides. Depending on the sample, the sum of hematite and goethite accounts for 38% (±6%) to 72% (±9%) of the total Fe. The lower value corresponds to dust samples from Bodélé (samples SOP0-4, SOP0-5, and SOP1-22), whereas the highest value corresponds to samples of Sahelian dust emitted locally in Banizoumbou (SOP1-17, SOP1-37, and SOP1-48). This means that iron associated with clays is predominant in the samples issued from Bodélé, accounting for 55% (±10%) of the total iron, whereas it represents only 29% (±2%) of the total iron in the Sahelian samples. The comparison with the independent estimate of the iron oxide content from the CBD extraction analysis is possible for seven samples, as shown in Table 5. The agreement is satisfactory. Differences between the two estimates are compatible within one standard deviation of the combined error, with the only exception being sample SOP0-4 of Bodélé dust, for which the apparent fraction of Fe attributed to iron oxides estimated by XANES is significantly lower than the value obtained by CBD, i.e., 38% (±6%) against 52% (±5%), respectively. Our estimates are also in agreement with *Lazaro et al.* [2008], who observed higher iron oxide content in Sahelian than in Saharan dust.

Table 4. Comparison of Expected Relative Abundances of Fe in Binary and Ternary Mixtures With Those Estimated From Least-Square Linear Regressions of First Derivatives of XANES Normalized Absorbance Spectra

	Expected Relative Abundances			Estimated Relative Abundances		
Sample ID	Hematite	Goethite	Illite	Hematite	Goethite	Illite
H50G50	0.53	0.48	---	0.56 (0.026)	0.44 (0.026)	---
H25G75	0.23	0.77	---	0.29 (0.029)	0.71 (0.026)	---
I30G30H30	0.46	0.50	0.04	0.45 (0.034)	0.50(0.029)	0.052 (0.019)

Table 5. Results of Least Squares Linear Combination Analysis of the XANES Spectra of Dust Samples[a]

		Apparent Fraction of Fe, XANES					Apparent Fe Oxide Fraction	
Sample ID	Origin	Illite	Goethite	Hematite	Montmorillonite	Nontronite	XANES	CBD
SOP0-4	PSA5 (Bodélé)	0.62 (0.02)	0.23 (0.03)	0.15 (0.03)	---	----	0.38 (0.06)	0.52 (0.05)
SOP0-5	PSA5 (Bodélé)	0.45 (0.02)	0.25 (0.02)	0.15 (0.03)	0.14 (0.04)	----	0.40 (0.05)	----
		0.38 (0.02)	0.21 (0.02)	0.16 (0.03)	----	0.26 (0.04)	0.36 (0.05)	----
SOP1-19	PSA5 (Bodélé/Sudan)	0.39 (0.02)	0.39 (0.03)	0.22 (0.03)	----	----	0.61 (0.06)	0.55 (0.06)
SOP1-22	PSA5 (Bodélé/Sudan)	0.53 (0.02)	0.31 (0.03)	0.10 (0.03)	0.06 (0.04)	----	0.41 (0.05)	----
		0.47 (0.03)	0.28 (0.03)	0.09 (0.03)	----	0.17 (0.05)	0.36 (0.05)	----
SOP0-38	PSA3	0.30 (0.02)	0.33 (0.02)	0.18 (0.03)	0.20 (0.04)		0.50 (0.05)	0.59 (0.06)
		0.25 (0.02)	0.31 (0.02)	0.20 (0.03)	----	0.25 (0.04)	0.50 (0.05)	----
SOP0-29	PSA3 + North Niger	0.38 (0.02)	0.42 (0.02)	0.20 (0.03)	----	----	0.62 (0.05)	0.65 (0.07)
SOP0-31	PSA3 + North Niger	0.29 (0.02)	0.29 (0.02)	0.24 (0.03)	0.17 (0.04)	----	0.53 (0.05)	----
		0.22 (0.02)	0.25 (0.02)	0.26 (0.03)	----	0.27 (0.04)	0.51 (0.05)	----
SOP0-46	PSA3 + traces of Sahelian dust from local erosion	0.25 (0.02)	0.33 (0.02)	0.23 (0.02)	0.19 (0.04)	----	0.56 (0.04)	----
		0.20 (0.02)	0.30 (0.02)	0.25 (0.02)	----	0.25 (0.04)	0.55 (0.05)	----
SOP1-15	PSA3 + traces of Sahelian dust from local erosion	0.39 (0.02)	0.43 (0.03)	0.18 (0.03)	----	----	0.62 (0.06)	0.51 (0.05)
SOP1-17	Sahelian dust, posterosion	0.28 (0.02)	0.45 (0.02)	0.26 (0.03)	----	----	0.72 (0.05)	0.64 (0.06)
SOP1-37	Sahelian dust, local erosion	0.28 (0.03)	0.45 (0.04)	0.26 (0.05)	----	----	0.72 (0.09)	0.70 (0.07)
SOP1-48	Sahelian dust, local erosion	0.32 (0.02)	0.49 (0.03)	0.18 (0.04)	----	----	0.68 (0.07)	----

[a]Columns 1–4 show the apparent fractions of Fe estimated for each mineral and the apparent Fe oxide fraction obtained by summing the apparent fractions attributed to hematite and goethite (column 5). When possible, this is compared with the Fe oxide fraction obtained by CBD analysis. Numbers in brackets are the absolute uncertainties estimated from the error returned by the least squares linear combination fit in the case of the XANES analysis and to the analytical errors in the case of the CBD results. Samples for which least squares linear combination analysis was performed once assuming the smectite in the form of montmorillonite, once in the form of nontronite, are reported twice.

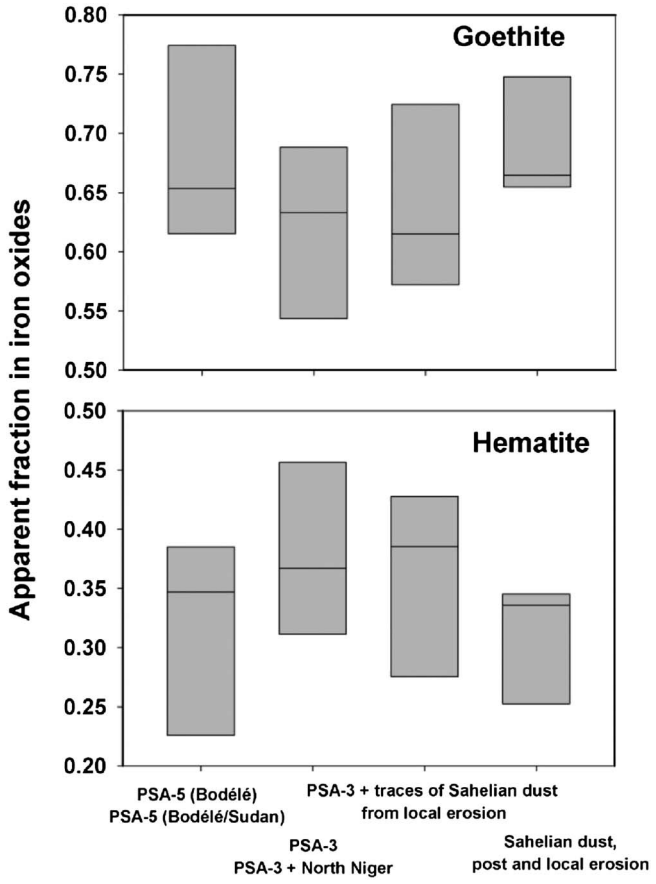

Figure 5. Box plots of the apparent fractions of goethite and hematite in iron oxides estimated by analysis of XANES spectra of samples sorted by estimated origin. The 5th, 50th, and 95th percentiles of the distributions of values are shown.

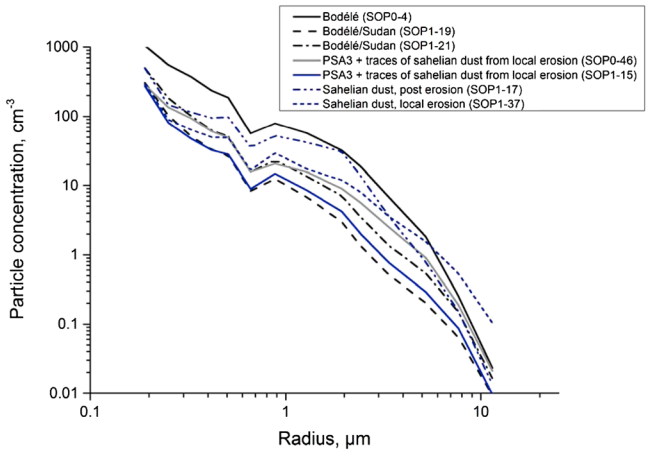

Figure 6. Mean number size distribution d*N*/dlog*r* for seven of the 12 samples investigated in this study.

The apparent fractions of Fe attributed to hematite and goethite in Table 5 can be converted to the apparent proportions of hematite and goethite in the iron oxides using the known Fe content in the standard samples as reported in Table 1.

Our results indicate that goethite accounts for 52% (±5) to 78% (±7) and hematite accounts for 22% (±3) to 48% (±5) of the total iron oxide mass. There is a difference in the mean values estimated separately for the dry season and the wet season samples (57% ±6 and 67% ±6, respectively). This is likely due to the local erosion samples, which are predominant during the wet season and which are richer in iron oxides than samples issued from PSA5 or PSA3. However, the dependence of the goethite and hematite content on the dust origin cannot be strictly established due to the low number of samples analyzed and to the large variability of the measured values when sorting them according to the expected source regions (Figure 5).

Table 6. Parameters of the Log-Fit Used to Approximate the Measured Number Size Distribution: r_g (in Nanometer) Represents the Median Diameter, σ_g is the Geometric Standard Deviation, and N_{tot} (in cm^{-3}) is the Total Aerosol Number Concentration

	M1	M2	M3	M4	M5	M6	M7	M8	M9
					SOP0-04				
N_{tot}	660	140	40	34	10	18	5	1.6	0.1
r_g	120	198	275	450	875	1200	1650	3000	5500
σ_g	1.4	1.6	1.3	1.2	1.2	1.5	1.3	1.4	1.4
					SOP1-19				
N_{tot}	200	36	2	4	2	1.4	0.5	0.16	0.026
r_g	120	198	275	450	875	1200	1650	3000	5500
σ_g	1.4	1.6	1.3	1.2	1.2	1.5	1.3	1.4	1.4
					SOP1-21				
N_{tot}	300	50	6	8	4	4	1	0.4	0.08
r_g	120	198	275	450	875	1200	1650	3000	5500
σ_g	1.4	1.6	1.3	1.2	1.2	1.5	1.3	1.4	1.4
					SOP0-46				
N_{tot}	200	50	6	8	3.2	4	1.4	0.8	0.08
r_g	120	198	275	450	875	1200	1650	3000	5500
σ_g	1.4	1.6	1.3	1.2	1.2	1.5	1.3	1.4	1.4
					SOP1-15				
N_{tot}	200	20	2	6	2.400	3	0.2	0.24	0.04
r_g	120	198	275	450	875	1200	1650	3000	5500
σ_g	1.4	1.6	1.3	1.2	1.2	1.5	1.3	1.4	1.4
					SOP1-17				
N_{tot}	400	40	2	24	4	14	4	1	0.04
r_g	120	198	275	450	875	1200	1750	3000	5500
σ_g	1.4	1.6	1.3	1.3	1.2	1.4	1.3	1.4	1.4
					SOP1-37				
N_{tot}	200	30	2	10	4	5	2	1.2	0.26
r_g	120	198	275	450	875	1200	1750	3000	5500
σ_g	1.4	1.6	1.3	1.2	1.2	1.4	1.3	1.4	1.5

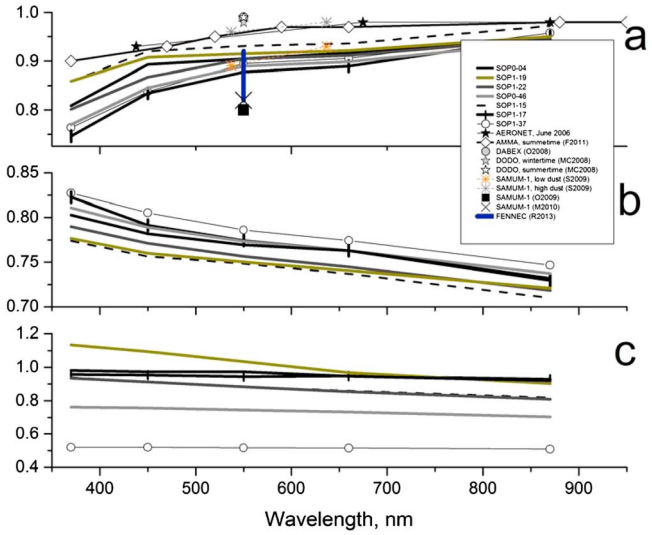

Figure 7. Single-scattering albedo, asymmetry factor and mass scattering efficiency ($m^2\ g^{-1}$) calculated with the measured goethite-to-hematite ratio (solid line). The single-scattering albedo values are compared to values published in the open literature. They are referenced as follows: O2008 = *Osborne et al.* [2008], MC2008 = *McConnell et al.* [2008], O2009 = *Otto et al.* [2009], S2009 = *Schladitz et al.* [2009], M2010 = *Müller et al.* [2010], F2011 = *Formenti et al.* [2011], and R2013 = *Ryder et al.* [2013]. Data are also compared to mean values for June 2006 obtained from the AERONET Sun photometer observations at the site of Banizoumbou.

It appears that the history of dust matters, in particular the height of transport. Having been transported close to the surface, dust-laden air masses could pick up dust from soils with different iron content and/or speciation during transit. It is nonetheless clear that these results have to be generalized to a larger number of samples, as well as to other source regions, in order to increase their significance.

At this point, a word of caution must be expressed on the capacity of the least squares fitting analysis of XANES spectra to quantify the relative proportions of hematite and goethite in mineral dust samples. Whereas the XANES spectra of oxide phases are significantly distinct from those of phyllosilicates, *O'Day et al.* [2004] have questioned the ability of distinguishing among the oxide phases because of the proximity of the position of peak edges and inflection points in their spectra. Nevertheless, it seems to us that the differences in the spectra both in the preedge (Figure 3) and in the XANES regions at approximately 7130 eV (Figure 2), as well as the success obtained in apportioning binary and ternary mixtures, demonstrate the ability to quantify the relative proportions of hematite and goethite in our samples.

It is also true that Fe oxyhydroxides or Fe phyllosilicates formed in soils might differ from those of standards minerals, both synthetic and natural. Al substitutions in hematite and goethite in tropical soils might reach up to 10 and 30% by mole, respectively [*Mendelovici et al.*, 1979; *Murad and Schwertmann*, 1988; *Wiriyakitnateekul et al.,* 2007]. This is the reason we have chosen, as much as possible, standards corresponding to the expected soil mineralogy of the investigated areas. The hematite standard, from Niger, has an iron content of 57% (by mass), lower than that expected from the stoichiometric formula (63%), suggesting that approximately 1% of Fe is substituted. The iron content of the goethite standard is 63%, lower by 9% than that expected from the stoichiometric formula (70% by mass). As a consequence, we might even be underestimating the apparent fraction of goethite in the samples.

3.2. Estimate of Optical Properties

Calculations of optical properties were performed on seven samples of dust originating in the Bodélé and Bodélé/Sudan regions (PSA5), locally from Banizoumbou, or representing mixing between long-range transport of Saharan dust from PSA3 and Sahelian dust picked up during transit.

The mean number size distributions corresponding to these filter samples are shown in Figure 6. The corresponding log-fit parameters (the median diameter r_g, the geometric standard deviation σ_g, and N_{tot} the total aerosol number concentration) used to initialize the Mie calculations are reported in Table 6. The modal median diameters are the same for all the distributions, but their relative intensities change. In particular, the coarse mode at 5.5 μm changes significantly and is most pronounced in the case of local emission of Sahelian dust (sample SOP1-37).

Results of the Mie calculations of the ω_0, g, and k_{ext} are shown in Figure 7. Values of the single-scattering albedo measured during the AMMA, DODO, DABEX, SAMUM, and FENNEC field campaigns [*McConnell et al.*, 2008; *Osborne et al.*, 2008; *Schladitz et al.*, 2009; *Otto et al.*, 2009; *Müller et al.*, 2010; *Formenti et al.,* 2011; *Ryder et al.*, 2013] are also shown for comparison. There is a certain spread in the calculated values; this derives both from

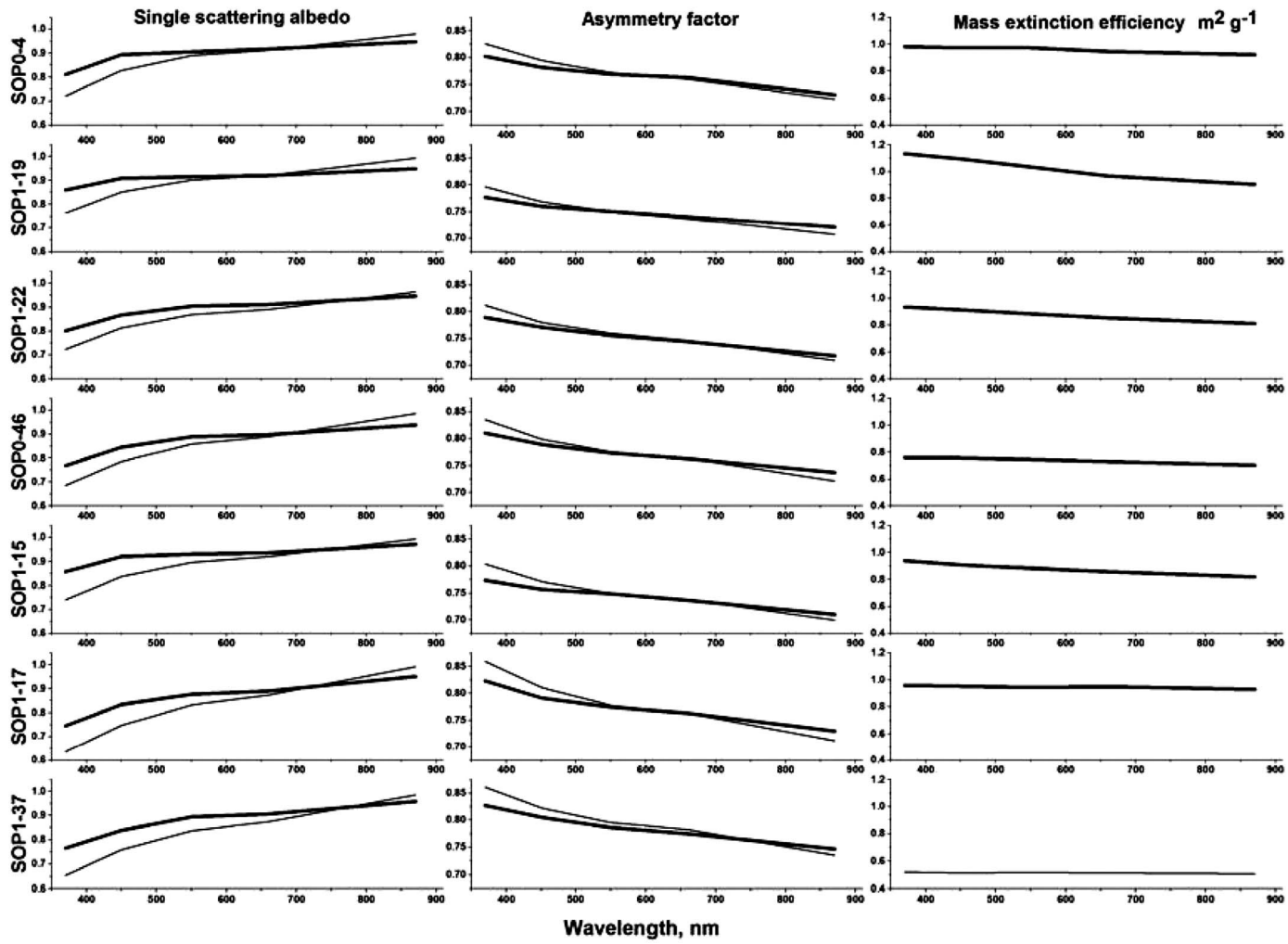

Figure 8. Comparison of single-scattering albedo, asymmetry factor, and mass scattering efficiency ($m^2\ g^{-1}$) calculated with the measured goethite-to-hematite ratio (solid thick line) and with the hematite (solid fine line).

the variability of the number size distribution and from the mineralogical composition. For the single-scattering albedo, the highest variability is at 370 nm, where ω_0 varies between 0.75 and 0.85. At 870 nm, the spread among values decreases and ω_0 varies between 0.95 and 0.98. At 550 nm, where most of the measurements are available, our estimates range between 0.89 and 0.93. These values are in the range of those measured during field campaigns; the SAMUM-1 and the FENNEC ones represent the lower bound and the AMMA, DODO, and DABEX represent the upper bound. Values of g vary between 0.78 and 0.83 at 370 nm and between 0.73 and 0.77 at 870 nm. Values of k_{ext} vary between 1.1 and 0.5 $m^2\ g^{-1}$, with limited spectral dependence.

All field data (ours included) were obtained for specific and differing atmospheric conditions. Therefore, it is difficult to assess whether differences are due to regional variability of the composition or to differences in the size distribution, or both. As already noted by *Klaver et al.* [2011], there is no systematic relation between the iron oxide content and/or the relative proportions of goethite and hematite and the magnitude of the single-scattering albedo, which will also depend on the complex refractive index of the dust matrix in which the iron oxides are embedded, on their mixing state and on their size distribution. This is does not contradict the conclusions of *Moosmüller et al.* [2012], who found a linear relationship between the single-scattering albedo and the elemental iron content in fine dust (mass fraction of particles of diameter smaller than 2.5 μm) but did not take into account the fact that not all the elemental iron is in the form of light-absorbing oxides.

To highlight the effect of representing the mineralogy of the iron oxides in mineral dust, Figure 8 shows the values of ω_0, g, and k_{ext} obtained by taking into account the relative proportions of hematite and goethite

compared to those calculated as if all the iron oxides were in the form of hematite. The predominance of goethite over hematite reduces the spectral dependence of the single-scattering albedo and the asymmetry factor. The single-scattering albedo increases at wavelengths below 660 nm (up 12%) but decreases slightly at 870 nm (within 3%). Conversely, the asymmetry factor is lowered below 550 nm (within 3%) and increases by 1% above. The mass extinction efficiency is unaffected by changes in the mineralogical composition.

4. Conclusions

Using nondestructive X-ray absorption on natural bulk samples of mineral dust emitted or transported over Western Africa, we were able to apportion elemental iron in mineral dust between illite, smectite clays, and iron oxides. We have shown that in the aerosol phase (as in soils), iron oxides are composed of goethite, an iron oxy(hydro)oxide, and hematite, both of which are in the Fe(III) oxidation state. Regardless of the source region, goethite is more abundant than hematite. Goethite and hematite are major light absorbers in the shortwave spectrum. Therefore, their partitioning is relevant to the direct effect of mineral dust on radiation, and their quantitative apportionment has to be taken into account by models predicting the direct radiative effect of mineral dust in the shortwave spectrum. In particular, a sensitivity study shows that the dominance of goethite over hematite reduces the single-scattering albedo in the UV region where dust can affect atmospheric photochemistry [*Casasanta et al.,* 2011]. Conversely, the partitioning between hematite and goethite is not important in the longwave, where iron oxides play a minor role in light absorption [*Di Biagio et al.,* 2014]. In the same way, the repartition between hematite and goethite is not relevant to estimating the iron fractional solubility in water [*Journet et al.,* 2008]; this is highly dependent on the position and oxidation states in each mineral lattice [*Shi et al.,* 2012]. The position of the preedge peak indicates the absence of Fe(II) minerals in our samples; this is in agreement with the poor solubility observed for African mineral dust at the source [*Paris et al.,* 2010, 2011]. This is also in agreement with various previous studies of soils as well as mineral dust aerosols transported towards urban areas [*Ohta et al*., 2006; *Prietzel et al*., 2007.

This research should be pursued in various ways. A systematic investigation of the regional variability of the mineralogy of the iron oxides is envisaged in order to increase the statistical representativeness of the current results, as well as to enlarge the number of source regions investigated. Furthermore, the study of the dependence of the goethite-to-hematite ratio on particle size will be pursued to improve the representation of the mineralogy of mineral dust in climate models.

Acknowledgments

Based on a French initiative, AMMA was built by an international scientific group and is currently funded by a large number of agencies, especially from France, the United Kingdom, the United States, and Africa. It was the beneficiary of a major financial contribution from the European Community's Sixth Framework Research Program. Detailed information on scientific coordination and funding is available on the AMMA International Web site at www.amma-international.org. Financial support by the API-AMMA French national funding programs is acknowledged. We acknowledge SOLEIL for provision of synchrotron radiation facilities (Proposal ID 20090570) and use of the Spectroscopy Applied to Material Based on Absorption (SAMBA) beamline. Thanks are also due to the LISA personnel who participated in field campaigns and helped with sample collection and to P. Goloub and B. Holben and all the members of the AERONET and PHOTONS groups for managing the Sun photometer network and providing high-quality data. All of the data used in this study are available from the first author upon email request.

References

Anderson, T. L., et al. (1996), Performance characteristics of a high-sensitivity, three-wavelength, total scatter/backscatter nephelometer, *J. Atmos. Oceanic Technol.*, *13*, 967–986.

Arimoto, R., W. Balsam, and C. Schloesslin (2002), Visible spectroscopy of aerosol particles collected on filters: Iron-oxide minerals, *Atmos. Environ.*, *36*, 89–96.

Balkanski, Y., M. Schulz, T. Claquin, and S. Guibert (2007), Reevaluation of mineral aerosol radiative forcings suggests a better agreement with satellite and AERONET data, *Atmos. Chem. Phys.*, *7*, 81–95, doi:10.5194/acp-7-81-2007.

Baron, P. A., and K. Willeke (2001), *Aerosol Measurement: Principles, Techniques and Applications*, 2nd ed., John Wiley, New York.

Barthelmy, D. (2007), Mineralogy database. [Available at http://www.webmineral.com, last accessed 2 January 2014.]

Bedidi, A., and B. Cervelle (1993), Light scattering by spherical particles with hematite and goethite like optical properties: Effect of water impregnation, *J. Geophys. Res.*, *98*, 11,941–11,952, doi:10.1029/93JB00188.

Bohren, C. F., and D. R. Huffman (1983), *Absorption and Scattering of Light by Small Particles*, Wiley, New York.

Boucher, O., et al. (2013), Clouds and aerosols, in *Climate Change 2013: The Physical Science Basis. Contribution of Working Group I to the Fifth Assessment Report of the Intergovernmental Panel on Climate Change*, edited by T. F. Stocker et al., pp. 571–658, Cambridge Univ. Press, Cambridge, U. K., and New York.

Briois, V., E. Fonda, S. Belin, L. Barthe, C. La Fontaine, F. Langlois, M. Ribbens, and F. Villain (2011), *UVX 2010 - 10e Colloque sur les Sources Cohérentes et Incohérentes UV, VUV et X, Applications et Développements Récents*, pp. 41–47, EDP- Sciences, Les Ulis, France.

Casasanta, G., A. G. di Sarra, D. Meloni, F. Monteleone, G. Pace, S. Piacentino, and D. Sferlazzo (2011), Large aerosol effects on ozone photolysis in the Mediterranean, *Atmos. Environ.*, *45*, 3937–3943.

Chýlek, P., and J. Wong (1995), Effect of absorbing aerosol on global radiation budget, *Geophys. Res. Lett.*, *22*, 929–931, doi:10.1029/95GL00800.

Claquin, T., M. Schulz, and Y. J. Balkanski (1999), Modeling the mineralogy of atmospheric dust sources, *J. Geophys. Res.*, *104*, 22,243–22,256, doi:10.1029/1999JD900416.

Di Biagio, C., H. Boucher, S. Caquineau, S. Chevaillier, J. Cuesta, and P. Formenti (2014), Variability of the infrared complex refractive index of African mineral dust: Experimental estimation and implications for radiative transfer and satellite remote sensing, *Atmos. Chem. Phys. Discuss.*, *14*, 10,597–10,657, doi:10.5194/acpd-14-10597-2014.

di Sarra, A., C. Di Biagio, D. Meloni, F. Monteleone, G. Pace, S. Pugnaghi, and D. Sferlazzo (2011), Shortwave and longwave radiative effects of the intense Saharan dust event of March 25–26, 2010, at Lampedusa (Mediterranean sea), *J. Geophys. Res.*, *116*, D23209, doi:10.1029/2011JD016238.

Dräger, G., R. Frahm, G. Materlik, and O. Brummer (1988), On the multipole character of the X-ray transitions in the pre-edge structure of Fe K absorption spectra. An experimental study, *Phys. Status Solidi B*, *146*, 287–294, doi:10.1002/pssb.2221460130.

Dubovik, O., B. Holben, T. F. Eck, A. Smirnov, Y. J. Kaufman, M. D. King, D. Tanré, and I. Slutsker (2002), Variability of absorption and optical properties of key aerosol types observed worldwide locations, *J. Atmos. Sci.*, *59*, 590–608.

Formenti, P., et al. (2008), Regional variability of the composition of mineral dust from western Africa: Results from the AMMA SOP0/DABEX and DODO field campaigns, *J. Geophys. Res.*, *113*, D00C13, doi:10.1029/2008JD009903.

Formenti, P., J. L. Rajot, K. Desboeufs, F. Saïd, N. Grand, S. Chevaillier, and C. Schmechtig (2011), Airborne observations of mineral dust over western Africa in the summer Monsoon season: Spatial and vertical variability of physico-chemical and optical properties, *Atmos. Chem. Phys.*, *11*, 6387–6410, doi:10.5194/acp-11-6387-2011.

Formenti, P., S. Caquineau, K. Desboeufs, A. Klaver, S. Chevaillier, E. Journet, and J. L. Rajot (2014), Mapping the physico-chemical properties of mineral dust in western Africa: Mineralogical composition, *Atmos. Chem. Phys. Discuss.*, *14*, 10,241–10,310, doi:10.5194/acpd-14-10241-2014.

Haywood, J. M., P. Francis, S. Osborne, M. Glew, N. Loeb, E. Highwood, D. Tanré, G. Myhre, P. Formenti, and E. Hirst (2003), Radiative properties and direct radiative effect of Saharan dust measured by the C-130 aircraft during SHADE: 1. Solar spectrum, *J. Geophys. Res.*, *108*(D18), 8577, doi:10.1029/2002JD002687.

Highwood, E. J., J. M. Haywood, M. D. Silverstone, S. M. Newman, and J. P. Taylor (2003), Radiative properties and direct effect of Saharan dust measured by the C-130 aircraft during Saharan Dust Experiment (SHADE): 2. Terrestrial spectrum, *J. Geophys. Res.*, *108*(D18), 8578, doi:10.1029/2002JD002552.

Hinds, W. C. (1999), *Aerosol Technology: Properties, Behavior, and Measurement of Airborne Particles*, 504 pp., John Wiley, Chichester, U. K.

Holben, B. N., et al. (1998), AERONET-A federated instrument network and data archive for aerosol characterisation, *Remote Sens. Environ.*, *66*, 1–16.

Journet, E., K. V. Desboeufs, S. Caquineau, and J.-L. Colin (2008), Mineralogy as a critical factor of dust iron solubility, *Geophys. Res. Lett.*, *35*, L07805, doi:10.1029/2007GL031589.

Journet, E., Y. Balkanski, and S. P. Harrison (2014), A new data set of soil mineralogy for dust-cycle modeling, *Atmos. Chem. Phys.*, *14*, 3801–3816, doi:10.5194/acp-14-3801-2014.

Karickhoff, S. W., and G. W. Bailey (1973), Optical absorption spectra of clay minerals, *Clays Clay Miner.*, *21*, 59–70.

Klaver, A., P. Formenti, S. Caquineau, S. Chevaillier, P. Ausset, G. Calzolai, S. Osborne, B. Johnson, M. Harrison, and O. Dubovik (2011), Physico-chemical and optical properties of Sahelian and Saharan mineral dust: In situ measurements during the GERBILS campaign, *Q. J. R. Meteorol. Soc.*, *137*, 1193–1210, doi:10.1002/qj.889.

Lafon, S., J. Rajot, S. Alfaro, and A. Gaudichet (2004), Quantification of iron oxides in desert aerosol, *Atmos. Environ.*, *38*, 1211–1218.

Lafon, S., I. N. Sokolik, J. L. Rajot, S. Caquineau, and A. Gaudichet (2006), Characterization of iron oxides in mineral dust aerosols: Implications for light absorption, *J. Geophys. Res.*, *111*, D21207, doi:10.1029/2005JD007016.

Lau, K. M., K. M. Kim, Y. C. Sud, and G. K. Walker (2009), A GCM study of the response of the atmospheric water cycle of West Africa and the Atlantic to Saharan dust radiative forcing, *Ann. Geophys.*, *27*, 4023–4037, doi:10.5194/angeo-27-4023-2009.

Laurent, B., B. Marticorena, G. Bergametti, J. F. Léon, and N. M. Mahowald (2008), Modeling mineral dust emissions from the Sahara desert using new surface properties and soil database, *J. Geophys. Res.*, *113*, D14218, doi:10.1029/2007JD009484.

Lazaro, F. J., L. Gutiérrez, V. Barrón, and M. D. Gelado (2008), The speciation of iron in desert dust collected in Gran Canaria (Canary Islands): Combined chemical, magnetic and optical analysis, *Atmos. Environ.*, *42*(40), 8987–8996.

Longtin, D. R., E. P. Shettle, J. R. Hummel, and J. D. Pryce (1988), A wind dependent desert aerosol model: Radiative properties, AFGLTR-88-0112, Air Force Geophys. Lab., Hanscom AFB, Mass.

Marticorena, B., B. Chatenet, J. L. Rajot, S. Traoré, M. Coulibaly, A. Diallo, I. Koné, A. Maman, T. Ndiaye, and A. Zakou (2010), Temporal variability of mineral dust concentrations over West Africa: Analyses of a pluriannual monitoring from the AMMA Sahelian Dust Transect, *Atmos. Chem. Phys.*, *10*(18), 8899–8915.

McConnell, C. L., E. J. Highwood, H. Coe, P. Formenti, B. Anderson, S. Osborne, S. Nava, K. Desboeufs, G. Chen, and M. A. J. Harrison (2008), Seasonal variations of the physical and optical characteristics of Saharan dust: Results from the Dust Outflow and Deposition to the Ocean (DODO) experiment, *J. Geophys. Res.*, *113*, D14S05, doi:10.1029/2007JD009606.

McConnell, C. L., P. Formenti, E. J. Highwood, and M. A. J. Harrison (2010), Using aircraft measurements to determine the refractive index of Saharan dust during the DODO Experiments, *Atmos. Chem. Phys.*, *10*, 3081–3098, doi:10.5194/acp-10-3081-2010.

Mehra, O. P., and M. L. Jackson (1960), Iron oxide removal from soils and clays by a dithionite-citrate buffered with sodium bicarbonate, *Clays Clay Miner.*, *7*, 317–327.

Mendelovici, E., S. Yariv, and R. Villalba (1979), Aluminum-bearing goethite in Venezuelan laterites, *Clays Clay Miner.*, *27*(5), 368–372.

Moosmüller, H., J. P. Engelbrecht, M. Skiba, G. Frey, R. K. Chakrabarty, and W. P. Arnott (2012), Single scattering albedo of fine mineral dust aerosols controlled by iron concentration, *J. Geophys. Res.*, *117*, D11210, doi:10.1029/2011JD016909.

Müller, T., A. Schladitz, A. Massling, N. Kaaden, K. Kandler, and A. Wiedensohler (2010), Spectral absorption coefficients and imaginary parts of refractive indices of Saharan dust during SAMUM-1, *Tellus, Ser. B*, *61*(1), 79–95.

O'Day, P. A., N. Rivera Jr., R. Root, and S. A. Carroll (2004), X-ray absorption spectroscopic study of Fe reference compounds for the analysis of natural sediments, *Am. Mineral.*, *89*, 572–585.

Ohta, A., H. Tsuno, H. Kagi, Y. Kanai, M. Nomura, R. Zhang, S. Terashima, and N. Imai (2006), Chemical compositions and XANES speciations of Fe, Mn and Zn from aerosols collected in China and Japan during dust events, *Geochem. J.*, *40*, 363–376.

Osborne, S. R., B. T. Johnson, J. M. Haywood, A. J. Baran, M. A. J. Harrison, and C. L. McConnell (2008), Physical and optical properties of mineral dust aerosol during the dust and biomass-burning experiment, *J. Geophys. Res.*, *113*, D00C03, doi:10.1029/2007JD009551.

Otto, S., E. Bierwirth, B. Weinzierl, K. Kandler, M. Esselborn, M. Tesche, A. Schladitz, M. Wendisch, and T. Trautmann (2009), Solar radiative effects of a Saharan dust plume observed during SAMUM assuming spheroidal model particles, *Tellus, Ser. B*, *61*(1), 270–296.

Paris, R., K. V. Desboeufs, P. Formenti, S. Nava, and C. Chou (2010), Chemical characterisation of iron in dust and biomass burning aerosols during AMMA-SOP0/DABEX: Implication for iron solubility, *Atmos. Chem. Phys.*, *10*, 4273–4282, doi:10.5194/acp-10-4273-2010.

Paris, R., K. V. Desboeufs, and E. Journet (2011), Variability of dust iron solubility in atmospheric waters: Investigation of the role of oxalate organic complexation, *Atmos. Environ.*, *45*, 6510–6517, doi:10.1016/j.atmosenv.2011.08.068.

Patterson, E. M., D. A. Gillette, and B. H. Stockton (1977), Complex index of refraction between 300 and 700 nm for Saharan aerosols, *J. Geophys. Res.*, *82*, 3153–3160, doi:10.1029/JC082i021p03153.

Prietzel, J., J. Thieme, K. Eusterhues, and D. Eichert (2007), Iron speciation in soils and soil aggregates by synchrotron-based X-ray micro-spectroscopy (XANES, μ-XANES), *Eur. J. Soil Sci.*, *58*, 1027–1041, doi:10.1111/j.1365-2389.2006.00882.x.

Prospero, J. M., P. Ginoux, O. Torres, S. E. Nicholson, and T. E. Gill (2002), Environmental characterization of global sources of atmospheric soil dust identified with the Nimbus 7 Total Ozone Mapping Spectrometer (TOMS) absorbing aerosol product, *Rev. Geophys.*, *40*(1), 1002, doi:10.1029/2000RG000095.

Querry, M. R., G. Osborne, K. Lies, R. Jordon, and R. M. Coveney (1978), Complex refractive index of limestone in the visible and infrared, *Appl. Opt.*, *17*, 353–356.

Rajot, J. L., et al. (2008), AMMA dust experiment: An overview of measurements performed during the dry season special observation period (SOP0) at the Banizoumbou (Niger) supersite, *J. Geophys. Res.*, *113*, D00C14, doi:10.1029/2008JD009906.

Ravel, B., and M. Newville (2005), ATHENA, ARTEMIS, HEPHAESTUS: Data analysis for X-ray absorption spectroscopy using IFEFFIT, *J. Synchrotron Radiat.*, *12*, 537–541.

Redelsperger, J.-L., C. D. Thorncroft, A. Diedhiou, T. Lebel, D. J. Parker, and J. Polcher (2006), African Monsoon Multidisciplinary Analysis: An international research project and field campaign, *Bull. Am. Meteorol. Soc.*, *87*, 1739–1746, doi:10.1175/BAMS-87-12-1739.

Ryder, C. L., et al. (2013), Optical properties of Saharan dust aerosol and contribution from the coarse mode as measured during the Fennec 2011 aircraft campaign, *Atmos. Chem. Phys.*, *13*, 303–325, doi:10.5194/acp-13-303-2013.

Scheuvens, D., L. Schütz, K. Kandler, M. Ebert, and S. Weinbruch (2013), Bulk composition of northern African dust and its source sediments—A compilation, *Earth Sci. Rev.*, *116*, 170–194, doi:10.1016/j.earscirev.2012.08.005.

Schladitz, A., T. Müller, N. Kaaden, A. Massling, K. Kandler, M. Ebert, S. Weinbruch, C. Deutscher, and A. Wiedensohler (2009), In situ measurements of optical properties at Tinfou (Morocco) during the Saharan mineral dust experiment SAMUM 2006, *Tellus, Ser. B*, *61*(1), 64–78.

Schwertmann, U. (1971), Transformation of hematite to goethite in soils, *Nature*, *232*, 624–625.

Seinfeld, J. H., and S. N. Pandis (1997), *Atmospheric Chemistry and Physics: From Air Pollution to Climate Change*, 1326 pp., John Wiley, New York.

Shao, Y., K.-H. Wyrwoll, A. Chappell, J. Huang, Z. Lin, G. H. McTainsh, M. Mikami, T. Y. Tanaka, X. Wang, and S. Yoon (2011), Dust cycle: An emerging core theme in Earth system science, *Aeolian Res.*, *2*, 181–204, doi:10.1016/j.aeolia.2011.02.001.

Shi, G. Y., H. Wang, B. Wang, W. Li, S. Gong, T. Zhao, and T. Aoki (2005), Sensitivity experiments on the effects of optical properties of dust aerosols on their radiative forcing under clear sky condition, *J. Meteorol. Soc. Jpn.*, *83A*, 333–346.

Shi, Z., M. D. Krom, T. D. Jickells, S. Bonneville, K. S. Carslaw, N. Mihalopoulos, A. R. Baker, and L. G. Benning (2012), Impacts on iron solubility in the mineral dust by processes in the source region and the atmosphere: A review, *Aeolian Res.*, *5*, 21–42, doi:10.1016/j.aeolia.2012.03.001.

Sinyuk, A., O. Torres, and O. Dubovik (2003), Combined use of satellite and surface observations to infer the imaginary part of refractive index of Saharan dust, *Geophys. Res. Lett.*, *30*(2), 1081, doi:10.1029/2002GL016189.

Slingo, A., H. E. White, N. A. Bharmal, and G. J. Robinson (2009), Overview of observations from the RADAGAST experiment in Niamey, Niger: 2. Radiative fluxes and divergences, *J. Geophys. Res.*, *114*, D00E04, doi:10.1029/2008JD010497.

Sokolik, I., and O. Toon (1999), Incorporation of mineralogical composition into models of the radiative properties of mineral aerosol from UV to IR wavelengths, *J. Geophys. Res.*, *104*, 9423–9444, doi:10.1029/1998JD200048.

Solmon, F., M. Mallet, N. Elguindi, F. Giorgi, A. Zakey, and A. Konaré (2008), Dust aerosol impact on regional precipitation over western Africa, mechanisms and sensitivity to absorption properties, *Geophys. Res. Lett.*, *35*, L24705, doi:10.1029/2008GL035900.

Torrent, J., U. Schwertmann, H. Fechter, and F. Alfarez (1983), Quantitative relationships between soil color an hematite content, *Soil Sci.*, *136*, 354–358.

Van Olphen, H., and J. J. Fripiat (1979), *Data Handbook for Clay Materials and Other Non-Metallic Minerals*, Pergamon Press, Oxford.

Washington, R., M. C. Todd, S. Engelstaedter, S. Mbainayel, and F. Mitchell (2006), Dust and the low-level circulation over the Bodélé Depression, Chad: Observations from BoDEx 2005, *J. Geophys. Res.*, *111*, D03201, doi:10.1029/2005JD006502.

Wilke, M., F. Farges, P.-E. Petit, G. E. J. Brown, and F. Mertin (2001), Oxidation state and coordination of Fe in minerals: An Fe K-XANES spectroscopic study, *Am. Mineral.*, *86*, 714–730.

Wiriyakitnateekul, W., A. Suddhiprakarn, I. Kheoruenromne, M. N. Smirk, and R. J. Gilkes (2007), Iron oxides in tropical soils on various parent materials, *Clays Clay Miner.*, *42*, 437–451, doi:10.1180/claymin.2007.042.4.02.